Fusion Engineering and Design 224 (2026) 115608

Contents lists available at ScienceDirect

Fusion Engineering and Design

journal homepage: www.elsevier.com/locate/fusengdes

Topology Optimization of a 10 T, 52 cm bore stellarator magnet structure

S. Del Nero [a,*], P. Fanelli [a], V. Prost [b], F.A. Volpe [b]

[a] Department of Economics, Engineering, Society and Business Organization (DEIM), University of Tuscia, Largo dell'Università, Viterbo, 01100, Italy
[b] Renaissance Fusion, 14 rue J. P. Timbaud, Fontaine, 38600, France

ARTICLE INFO

Keywords:
Stellarator
High magnetic field
Wide HTS magnets
Structural design
Topology optimization

ABSTRACT

The performance of high-field magnets is increasingly constrained not by the limits of High-Temperature Superconducting materials, but by the structural systems needed to withstand the intense Electro-Magnetic forces they produce. In response to this challenge, this work presents a design-driven methodology for optimizing the reinforcement structures of 52 cm bore wide HTS magnets under development at Renaissance Fusion, aimed at achieving magnetic fields up to 10 T on the plasma axis. A custom Topology Optimization tool, based on the Solid Isotropic Material Penalization method and implemented entirely in PyMAPDL, was employed to guide the mechanical design of the magnet reinforcements. Starting from a large design domain (∼11.3 tons per sector), Topology Optimization with varying volume fractions produced lightweight structures, down to 3.93 tons, that meet strict mechanical constraints on magnet displacement (<1 mm), magnet strain (<0.5%) and global stress (<800 MPa). Then, a second optimization stage using extrusion constraints methodologies was employed to further optimize the structure while ensuring manufacturability. Recurring features from these runs informed the development of a parametric model, enabling further refinement and a final mass of 1.20 t. The final structure, segmented into sub-components for a feasible assembly procedure, retained the required mechanical performance while ensuring ease of manufacturing using conventional processes. This magnet design demonstrate the applicability and benefits of our multi-stage constrained topology optimization method for advancing the structural design of high-field and compact stellarators.

1. Introduction

In recent years, Topology Optimization (TO) has emerged as a powerful tool in structural design, particularly in fields such as aerospace, automotive, and biomedical engineering [1–3]. The TO strength lies in the ability to generate efficient, lightweight, and mechanically robust structures by systematically distributing material within a defined design space, often finding non-intuitive solutions that would be difficult to achieve through traditional design approaches. However solutions generated by TO are often highly complex and not directly compatible with traditional manufacturing methods. As a result, the integration of manufacturing constraints into the TO workflow has become a critical area of research [4,5]. Without such constraints, which limit the space of admissible solutions, the optimized geometry may be difficult or even impractical to fabricate, requiring significant manual effort and time to convert the result into a clean engineering solution.

In the context of nuclear fusion, TO has demonstrated its potential in addressing both thermal and structural engineering challenges. For example, in the development of the Helical fusion reactor [6]; here, researchers applied TO to redesign the coil support structures. This approach led to a significant weight reduction of more than 25% compared to conventional designs. Subsequent static and seismic analyzes confirmed the structural integrity of the optimized supports. TO has also been utilized to determine optimal placements and orientations of permanent magnets in stellarators [7]; this method aims to simplify coil designs while maintaining effective plasma confinement, potentially reducing manufacturing complexity and enhancing performance. Researchers have also employed thermal TO to design plasma-facing components, such as the divertors [8]. By optimizing the distribution of the high thermal conductivity material within these components, the designs achieve improved thermal performance and structural resilience under extreme operating conditions. Further research applied TO to design tungsten-copper structures for plasma-facing component applications [9]. This approach improves the thermal and mechanical performance of components exposed to high heat fluxes, ensuring durability and efficiency in fusion reactor environments. The integration of automated parameter, shape, and TO techniques has been also explored in the design of divertors [10].

* Corresponding author.
E-mail address: simone.delnero@unitus.it (S. Del Nero).

https://doi.org/10.1016/j.fusengdes.2025.115608
Received 6 November 2025; Received in revised form 9 December 2025; Accepted 26 December 2025
Available online 3 January 2026

The development of next-generation stellarator experiments presents increasingly structural engineering challenges. Compact devices operating at high magnetic fields require highly optimized mechanical supports and reinforcements capable of withstanding extreme Electro-Magnetic (EM) loads without compromising manufacturability and system performance. Several fusion projects (both stellarators and tokamaks) have indeed highlighted that the peak stresses within coil support structures often approach the limits of structural materials [11–13].

In this work, we present a comprehensive TO workflow, developed entirely in PyMAPDL [14], for the conceptual design of reinforcements for Renaissance Fusion [15] simplified stellarator magnets based on laser engraved wide HTS conductors [16]. Unlike previous studies, which have focused on traditional HTS configurations, where reinforcement strategies follow relatively well-established structural design principles, our work addresses a novel challenge: non-uniform loads on wide HTS tapes. This non-standard geometry significantly alters the mechanical load paths and creates new constraints on how reinforcement structures must be designed, assembled, and supported.

To tackle this, we developed a new methodology combining a novel implementation of simultaneous multi-directional extrusion constraints, iterative refinement of the design domain based on material efficiency, and a parametric study to translate TO outputs into manufacturable components. This approach enables the systematic exploration of lightweight, stiff, and robust reinforcement topologies capable of withstanding extreme EM forces. Beyond identifying efficient reinforcement topologies, a key goal of this work is to ensure that the proposed structures can be translated into a manufacturable design. Particular attention is therefore given to incorporating manufacturing constraints and to developing an assembly strategy that bridges the gap between topology-optimized concepts and engineering solutions.

Here we apply this new TO method to 10 T stellarator magnet. For this first test application, we consider a hypothetical device of the same size and approximate geometry of an actual small test device under consideration at Renaissance Fusion. However, to translate this to reactor relevant parameters, the field was scaled to 10 T on the plasma axis and therefore much higher forces are developed compared to the actual device. Also note that the coils lie on cylinders (see Fig. 1), whereas in future embodiments they might lie on slanted cylinders, which would require a revised TO. The device considered in this study can be regarded as a scaled version of the W7X-like stellarator in Germany [17], with the difference that the coil winding surface is piece-wise cylindrical rather than fully conformal to the plasma boundary. While this approach simplifies coil manufacturing, it introduces a non-uniform current distribution and, consequently, strong spatial variations in the EM forces that must be addressed by the structural reinforcements.

The paper is organized as follows: Section 2 introduces the magnet system and corresponding EM loads. Section 3 provides a theoretical background on Topology Optimization, including the implementation of extrusion-based constraint. Section 4 discusses the initial, non-optimized structural model and outlines the key assumptions guiding the design. Section 5 presents the application of Topology Optimization to the magnet reinforcements and details the developed workflow up to the final conceptual structural design.

2. The magnet system

A new class of stellarator magnets are being developed by Renaissance Fusion based on laser engraved wound HTS tapes. These magnets are designed to generate a target magnetic field of 10 T on the plasma axis, with a corresponding peak magnetic field of 15.8 T on the coil windings. Such high field results in substantial EM forces, placing significant mechanical demands on the supporting and reinforcement structures. To estimate the magnitude of these loads, the magnet can be approximated as a simplified helical solenoid. Using standard expression from electromagnetic theory, the magnetic pressure P exerted by a magnetic field can be calculated as:

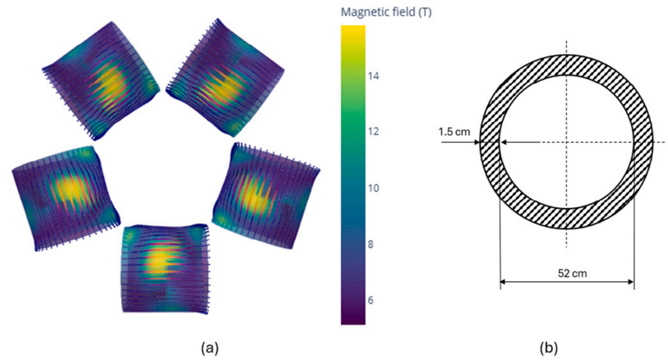

Fig. 1. (a) Top view of magnet arrangements with magnetic field distribution; (b) Magnet cross-section (not drawn to scale).

Table 1
Key parameters of the magnet.

Magnetic field on plasma axis, B_0	10 T
Peak magnetic field on coil windings	15.8 T
Magnet axial length	50 cm
Magnet diameter	52 cm
Radial centroid position	65 cm
Toroidal spacing	72°
HTS tape thickness	0.1 mm
Total winding thickness	1.5 cm
Number of magnets	5

$$P = \frac{B_0^2}{2\mu_0} \tag{1}$$

where B_0 is the magnetic field on the cylinder axis and μ_0 is the vacuum permeability ($\mu_0 = 4\pi 10^{-7}$ Tm/A). Assuming $B_0 = 10$ T at the plasma axis, the resulting uniform magnetic pressure on the windings is on the order of 40 MPa. This pressure generates substantial hoop and radial stresses that must be contained by structural supports to prevent failure or excessive deformation. The main parameters of the magnet considered in this study are summarized in Table 1.

The mechanical challenge becomes even more complex when considering the overall magnet arrangement and load distribution. Five magnets will be positioned along a pentagonal path, as shown in Fig. 1, and will have a cylindrical shape, with an axial length of 50 cm and a diameter of 52 cm. The EM loads generated by the combination of the magnetic field **B** and the density current **J** produce an antisymmetric distribution, with an order of magnitude higher than 40 MPa, reaching peaks of several hundreds of MPa (see unwrapped cylindrical map of EM loads in Fig. 2). Radially, the centroids of each magnet are 65 cm and are equally spaced in the toroidal direction of 72°. Each magnet will be composed of wide HTS tapes with a thickness of 0.1 mm, forming a total thickness of 1.5 cm. The HTS laser engraved wide tapes will be wrapped on a former and we assumed the same thickness as the magnets for initial modeling. The former must carry and sustain the inward loads that come from the magnet, while the outer reinforcement structure must yield the loads pointing outward.

3. Stiffness maximization problem under volume and extrusion constraints

In order to optimize the material distribution of the magnet structure, our approach maximizes the overall structural stiffness ensuring manufacturability and acceptable mechanical displacements, strains, and stresses. Among all the manufacturing constraints that can be

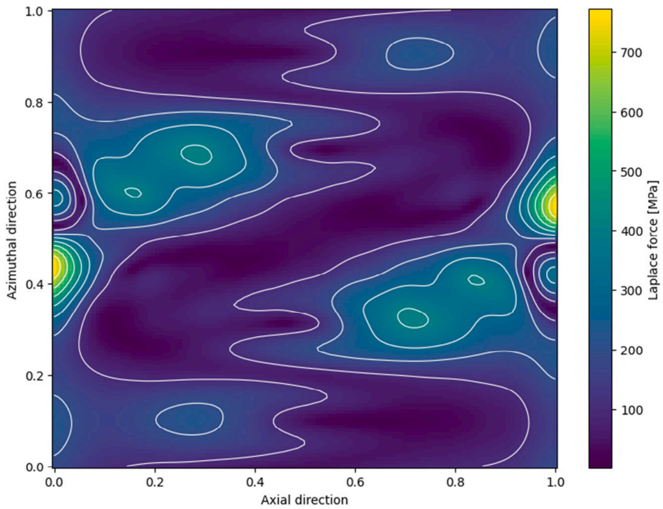

Fig. 2. Two-dimensional distribution of the Laplace force magnitude [MPa], with axes normalized w.r.t. the magnet's axial and poloidal directions.

imposed in TO, the extrusion constraint is particularly relevant due to its ability to provide clearer and feasible designs [5,18,19] that can be more readily fabricated through conventional processes such as welding of plates or casting. The TO with extrusion constraints was implemented as a constrained minimum compliance problem:

$$\begin{aligned} \min_{\rho} \quad & C(\tilde{\rho}) = \mathbf{U}^T \mathbf{K}(\tilde{\rho})\mathbf{U} = \sum_{i=1}^{e_{\mathrm{tot}}} \tilde{\rho}_i^p E_0 \mathbf{u}_i^T \mathbf{k}_{i,0}\mathbf{u}_i \\ \text{s.t.} \quad & \mathbf{K}(\tilde{\rho})\mathbf{U} = \mathbf{F} \\ & G_{\mathrm{v}} = \frac{\sum_{i=1}^{e_{\mathrm{dd}}} \tilde{\rho}_i \cdot v_i}{f \cdot V_0} - 1 \le 0 \\ & \tilde{\rho}_i = \tilde{\rho}_j, \quad \forall i,j \in C_k, \quad k = 1,2,\ldots,l \\ & \rho_{\min} \le \rho_i \le 1, \quad \forall i \in \Omega_{\mathrm{dd}} \end{aligned} \tag{2}$$

where ρ is the non-filtered element density vector, $\tilde{\rho}$ is the filtered element density vector, $C(\tilde{\rho})$ is the total structural compliance, $\mathbf{U}$ is the nodal displacement vector, $\mathbf{K}(\tilde{\rho})$ is the global element stiffness matrix, $E_{0,i}$ is the Young's modulus of solid material, $\mathbf{u}_i$ is the element nodal displacement vector, $\mathbf{k}_{i,0}$ is the unit element stiffness matrix, $\mathbf{F}$ is the external force vector, G_{v} is the global volume constraint, v_i is the ith element volume, f is the volume fraction, V_0 is the total volume of the design domain (Ω_{dd}), e_{tot} is the total number of elements, e_{dd} is the total number of elements in the design domain, C_k is the kth extrusion element column, $\rho_{\min}$ is the minimum element density. $\mathbf{K}(\tilde{\rho})\mathbf{U} = \mathbf{F}$ is the equilibrium equation that is solved at each TO iteration.

To obtain a meaningful distribution of material within the design domain, an interpolation scheme is required to distinguish between solid and void regions. A widely adopted approach is the Solid Isotropic Material with Penalization (SIMP) method [20], which discourages intermediate material densities by penalizing them during the optimization process, as they contribute less to structural performance. In SIMP, the stiffness matrix of each element, $\mathbf{k}_i(\tilde{\rho}_i)$, is expressed as a function of the element density $\tilde{\rho}_i$ and the stiffness of a fully dense element $\mathbf{k}_{i,0}$. This is achieved by interpolating the Young's modulus $E_i(\tilde{\rho}_i)$ as:

$$E_i(\tilde{\rho}_i) = \tilde{\rho}_i^p \cdot E_{0,i} \tag{3}$$

where p is the penalization factor (typically $p \ge 3$). This formulation promotes a clear 0–1 material distribution, encouraging elements to converge toward either solid or void states.

To accurately define the extrusion direction in the optimization process, the formulation (Eqs. (2)) is tailored for ordered meshes generated using a sweep method, in which source and target surfaces are clearly identifiable. In other words, the finite element mesh is firstly defined on the source surface and then extruded along a specific curve path.

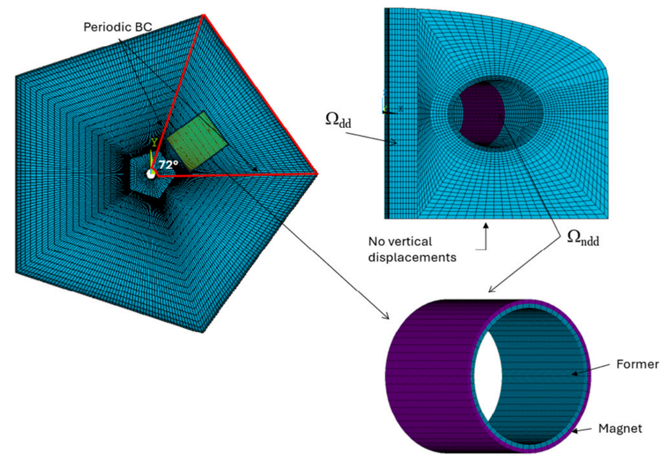

Fig. 3. Structural FE model of magnet (Ω_{ndd}), former (Ω_{ndd}) and design domain (Ω_{dd}).

This property is particularly useful when introducing the extrusion constraint, since the elements are consequently arranged in the same manner. In this way, several extrusion directions can be identified based on the element-connectivity. In particular, the extrusion directions based on the element connectivity can be formulated as a square binary matrix [21]:

$$H^{ij}_{\mathrm{extrusion}} = \begin{cases} 1, & \text{if elements } i \text{ and } j \in C_k, \\ 0, & \text{otherwise.} \end{cases} \tag{4}$$

which is used to modify and average the objective function gradient of each column of elements sharing the same extrusion direction.

The extrusion constraint is enforced at each TO iteration by modifying the element densities $\tilde{\rho}_j$ within each extrusion column C_k, ensuring that all elements in the column share the same density value as the corresponding base element $\tilde{\rho}_i$ (i.e., the element located on the selected source surface).

4. Finite Element model of initial non-optimized structure

The structural Finite Element (FE) model consists of two concentric cylinders (magnet and former) which represent the non-design domain Ω_{ndd} surrounded by a larger domain that defines the so called design domain region Ω_{dd} where the material must be removed, as shown in Fig. 3.

The initial mass considering both Ω_{ndd} and Ω_{dd} is about 11.3 tons. Both the former and the design domain are assumed to be made of SS316LN ($E = 200$ GPa, $\nu = 0.3$), a material widely adopted in cryogenic structural applications due to its favorable combination of mechanical performance and manufacturability. This steel is widely used in large-scale fusion systems such as ITER. At cryogenic temperatures, which match the operating range of the structure, this material exhibits a yield strength of around 1000 MPa at 4 K [22], making it particularly suitable for high-field, mechanically demanding environments such as this one.

The HTS magnets are composed of several layers of different materials, which are commonly a Hastelloy C-276 substrate (65%–75% of total HTS thickness), a buffer layer (2%–5%), a REBCO superconducting layer (1%–2%), a stabilizer layer made of copper (15%–25%) and an optional encapsulation layer (0%–10%). Since a final HTS composition has not yet been specified, this multilayer configuration is based on representative architectures commonly found in existing commercial HTS tapes [23]. Because of this multilayer structure, the mechanical behavior of HTS materials is highly anisotropic, making direct modeling challenging, specifically with the various geometric scales. To

Table 2
Equivalent mechanical properties of homogenized HTS material.

E_r	115 GPa
E_θ	141 GPa
E_z	141 GPa
$G_{r\theta}$	44 GPa
$G_{\theta z}$	54 GPa
$\nu_{r\theta}$	0.3
$\nu_{\theta z}$	0.3

address this, a homogenization technique was applied, allowing the magnet to be modeled as a transversely isotropic material [24–26]. In this model, mechanical properties are assumed to be constant in the plane of the HTS tape and variable in the out-of-plane (radial) direction. The following material parameters were defined for the HTS: radial (E_r), tangential (E_θ) and axial (E_z) Young's moduli; in-plane ($G_{r\theta}$) and out-of-plane ($G_{\theta z}$) shear moduli, in-plane ($\nu_{r\theta}$) and out-of-plane ($\nu_{\theta z}$) Poisson's ratios (see Table 2 for HTS equivalent mechanical properties).

Although the magnets will operate at cryogenic temperatures around 20 K, thermal contraction effects and thermomechanical loads have not been included in the present work. This assumption is justified by the focus of the study on EM load-bearing optimization during the early conceptual design phase, where stiffness and material distribution are the primary concerns. Moreover, in high-field fusion magnets, EM loads generally dominate the mechanical response.

Due to the periodic symmetry of the EM loads produced by the magnets, the resulting forces generated by each coil are directed radially inward toward the central axis and repeat every 72°. This periodicity allows structural analysis and TO to be performed in a single representative sector, significantly reducing computational cost without sacrificing accuracy. The EM loads were mapped onto the inner magnet surface using ANSYS Workbench's interpolation tools. The components of the original loads for the first magnet are $F_x = -4.96$ MN and $F_y = -3.61$ MN, respectively. Due to the mentioned periodicity of the loads, the total net force and resulting moment, when considering all modules, are zero, ensuring global static equilibrium.

The interaction between the former and the magnet, as well as between the magnet and the design domain, was initially modeled using bonded contacts. This simplification is appropriate for the early conceptual design stage, where the focus is on exploring optimal material distribution for structural stiffness and mass efficiency. Although bonded contacts may slightly overestimate load transfer efficiency and potentially increase local stress concentrations in the magnet, they allow for a more stable and computationally efficient simulation. Frictional contact, while more realistic for detailed mechanical behavior, was intentionally not implemented due to its high computational cost and slow convergence behavior, which can be prohibitive in iterative TO workflows. Regarding boundary conditions, the periodic nature of the geometry was enforced by applying periodic symmetry on the two lateral faces of the 72° sector, and constraint to prevent the vertical displacement were applied at the base of the design domain (see Fig. 3).

The displacement and stress fields of the initial non-optimized structure is shown in Figs. 4 and 5. The maximum displacement, that is lower then 1 mm, occurs in the magnet, while the most stressed components is the former which exhibits a peak stress about 530 MPa; furthermore, most of the stress is observed around the magnet and on its front side, reflecting the directional nature of the applied EM loads. An important safety parameter for the magnet is the longitudinal strain (along the tape-wrapping direction), which must be kept below 0.4–0.5% [27] to prevent irreversible degradation of the HTS material's current-carrying capacity. Although tangential strain is typically used in the assessment of narrow HTS tapes, in this study we opted to evaluate the equivalent strain. This choice reflects the consideration

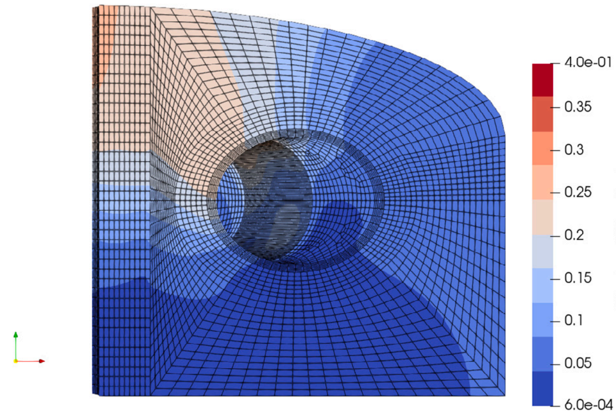

Fig. 4. Displacement field [mm] of initial non-optimized structure.

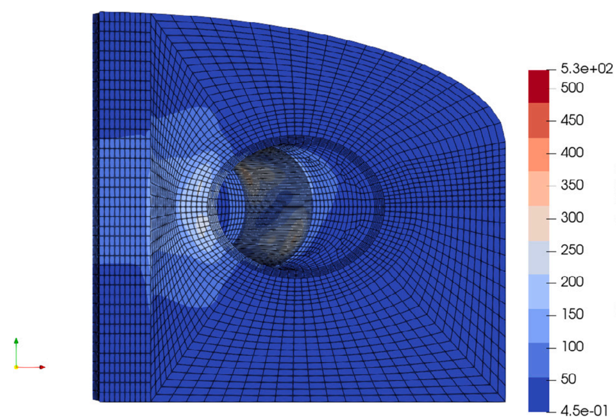

Fig. 5. Stress field [MPa] of initial non-optimized structure.

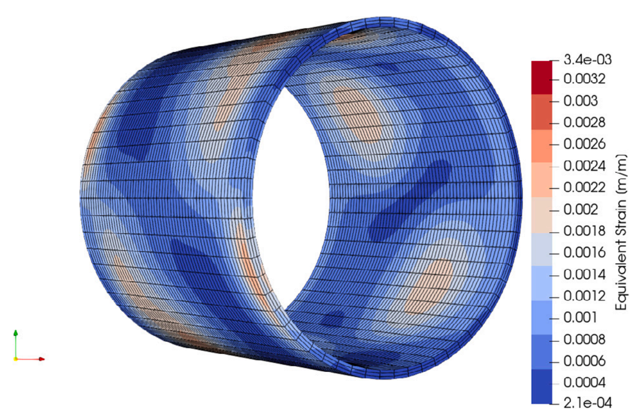

Fig. 6. Equivalent strain field [m/m] of magnet (initial non-optimized structure).

that in wide HTS tapes, deformation components in all directions can contribute to mechanical degradation. Moreover, to the best of our knowledge, there is lack of data or established criteria available in the literature for strain limits in wide HTS. Therefore, the equivalent strain offers a conservative and holistic metric for evaluating the mechanical behavior of the superconducting winding. In this case, the maximum equivalent strain in the magnet is about 0.34% (see Fig. 6), while the maximum stress on the magnet is about 410 MPa (see Fig. 5).

5. Conceptual design of magnet's reinforcements

The TO process for the design of the magnet's reinforcements was conducted in an iterative and hierarchical manner to progressively refine the material layout within the design domain. In the initial stage, the entire design domain was explored using a classical stiffness maximization approach with only a volume constraint. This allowed the optimizer to identify the general load paths and primary structural features needed to withstand the EM loads. Based on the outcome of this first optimization, a more compact design domain was defined, excluding regions consistently identified as non-essential in the initial iteration. This updated domain was then used as the starting point for a second optimization run incorporating extrusion constraints, enabling the identification of key reinforcement patterns. Following this second iteration, a parametric model was developed by extracting and combining the key structural features observed in both TO outcomes. This model was used to refine and formalize the design, enabling controlled variation of geometrical parameters and further guiding the development of a manufacturable and mechanically robust solution.

Although mechanical limits were not explicitly included in the optimization formulation, the solutions presented in this work were selected to satisfy a conservative global stress limit of 800 MPa, a maximum magnet displacement of 1 mm and a maximum magnet strain of 0.5%. The effect of such displacements on magnetic field errors will be investigated in future studies. We emphasize that the 800 MPa stress limit is applied globally across all structural components considered in the topology optimization, rather than being specific to the SS316LN former or the HTS layer. This global constraint ensures that no region of the optimized reinforcement experiences stresses exceeding conservative material bounds under the EM loads.

5.1. Maximum stiffness of initial model s.t. volume constraints

Three different volume fraction constraints were investigated: 30%, 20%, and 10%. These cases allowed for a comparative analysis of how material layout impacts the overall mechanical performance in terms of displacement, strain and stress. The outcomes are summarized in Table 3.

All resulting outcomes exhibited a similar qualitative behavior: material was mainly distributed around the magnet, forming a continuous reinforcement structure that resisted the EM forces. Notably, none of the configurations developed gravity support-like features, which is consistent with the nature of the net EM load being directed radially toward the machine center, and thus self-balanced in the full assembly.

Quantitatively, the solution at 30% volume fraction yielded a maximum displacement of 0.62 mm located on the magnet, a maximum equivalent strain of approximately 0.34% (also within the magnet), and a peak von Mises stress of 540 MPa in the former. The corresponding maximum stress within the magnet itself is 411 MPa. Reducing the volume fraction to 20% resulted in an increase in displacement to 0.81 mm and a slight increase in former stress to 566 MPa, with the magnet stress again reaching 422 MPa. The maximum equivalent strain remained essentially unchanged at 0.34%. Finally, under the most aggressive volume constraint of 10%, the maximum displacement increased to 1.5 mm, the equivalent strain in the magnet to 0.36%, and the peak stress in the former reached 692 MPa. The corresponding magnet stress in this case is 463 MPa. Figs. 7, 8, and 9 present the element density distributions obtained at the end of each TO run. In these figures, the non design regions are depicted in yellow.

5.2. Maximum stiffness of optimized model s.t. volume and extrusion constraints

Based on the obtained results in Section 5.1, a new starting geometry (3.93 t) was defined to initiate the next stage of optimization (see Fig. 10). To simplify the shape while retaining key structural features,

Table 3
Mechanical response of initial model under varying volume constraints. f: volume fraction; m_{final}: final mass; $u_{mag.}$: magnet maximum displacement; $\varepsilon_{mag.}$: maximum magnet strain; σ_{max}: maximum global stress.

f [%]	m_{final} [t]	u_{mag} [mm]	$\varepsilon_{mag.}$ [%]	σ_{max} [MPa]
30	3.20	0.62	0.34	540
20	2.30	0.81	0.34	566
10	1.30	1.50	0.36	692

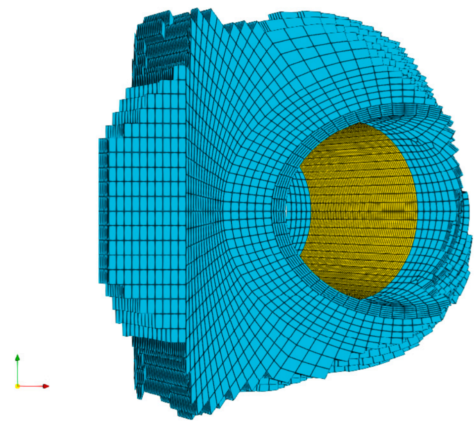

Fig. 7. Element density plot of initial topology optimized model with 30% of volume fraction (m_{final} = 3.20 t).

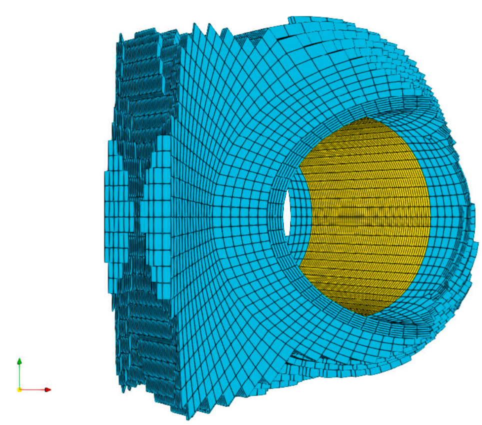

Fig. 8. Element density plot of initial topology optimized model with 20% of volume fraction (m_{final} = 2.30 t).

the material distribution from the first TO was projected onto the magnet's cross-sectional plane. This projection was then used to delineate the new design boundary. For clarity and manufacturability, the boundary was reconstructed using a B-spline representation controlled by a limited number of points, allowing the complexity of the geometry to be reduced.

Following the methodology described in Section 3, several optimizations were performed by progressively modifying the extent of the non-design domain around the magnet and adjusting the volume fraction accordingly. This approach was adopted to assess how the imposed non-design domain influences the final material distribution and to better understand the impact of its size on the optimized structural layout. The volume fraction adjustment ensured that all design cases resulted in comparable total masses, maintaining a consistent baseline for performance comparison. As in the previous analysis, each solution was evaluated in terms of material distribution, displacements, equivalent strains, and von Mises stresses, with particular attention paid to the structural response of the magnet.

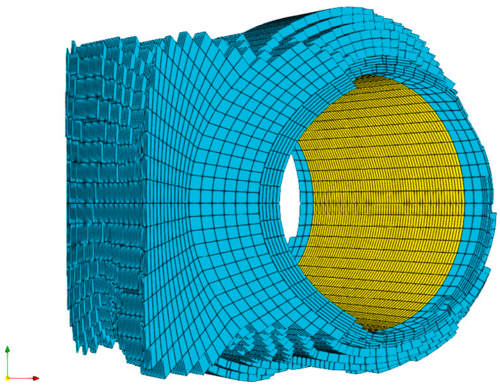

Fig. 9. Element density plot of initial topology optimized model with 10% of volume fraction ($m_{final} = 1.30$ t).

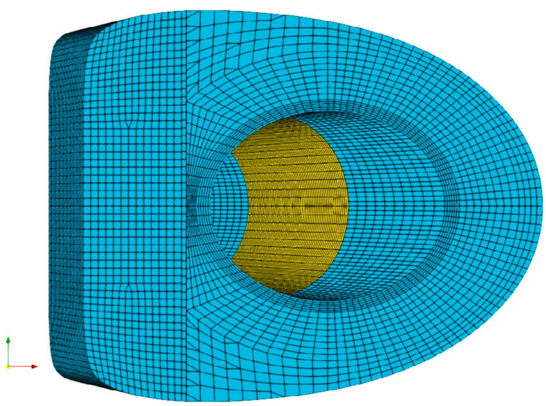

Fig. 10. Reconstructed design domain for second-stage optimization.

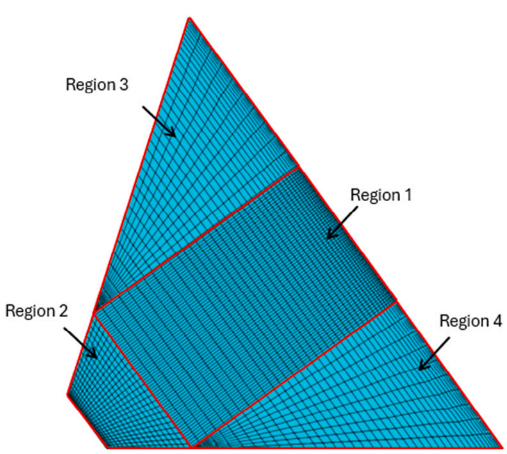

Fig. 11. Extrusion regions. Regions 2-3-4: extrusion constraint along toroidal direction; Region 1: extrusion constraint along magnet radial direction.

The extrusion constraints were enforced simultaneously by partitioning the design domain into several distinct regions as shown in Fig. 11, each assigned to a specific extrusion direction. In more detail, the extrusion directions are radial (normal to the cylindrical magnet surface) for Region 1, and axial (along magnet axis) for Region 2-3-4. This method of enforcing multiple different extrusion directions enables more practical and manufacturable designs while preserving optimization flexibility and mechanical performance.

Table 4
Topology optimization results for different extrusion constraints. Here, n_{layers} denotes the number of extrusion layers and f the applied volume fraction. Reported values include final mass m_{final}, maximum magnet displacement $u_{mag.}$, equivalent strain $\varepsilon_{mag.}$, and maximum stress σ_{max}.

n_{layers}	f [%]	m_{final} [t]	$u_{mag.}$ [mm]	$\varepsilon_{mag.}$ [%]	σ_{max} [MPa]
3	50	1.89	0.64	0.37	620
	37.5	1.57	1.30	0.36	720
	25	1.17	1.60	0.47	886
6	45	1.99	0.62	0.36	600
	31	1.58	0.83	0.37	710
	17	1.22	0.88	0.38	793
9	36	1.94	0.57	0.34	620
	21	1.62	0.60	0.35	670
	5	1.33	0.65	0.37	780

To constrain the model, one node of the design domain has been constrained in both toroidal and vertical directions, while bonded contacts have been again applied between each body in the FE model. The analyzed cases are shown in the first and second columns of Table 4. Here, n_{layers} is the number of layers and it is referred to the number of elements that surround the magnet and belong to the non design domain during TO process. The elements around the magnet are largely uniform in the direction normal to its respective outer surface, but tend to contract in Region 2. Approximately each layer of elements has a thickness of 1.6 cm.

The optimized material distributions are presented in Fig. 12. As shown in Fig. 12a–d, TO consistently promotes the formation of rib-like structures surrounding the magnet, providing enhanced stiffness along critical load paths. Additionally, all solutions consistently retain material at the front side of the magnet, as clearly illustrated in Fig. 12f. This recurring feature highlights its structural importance across different configurations and suggests the necessity of incorporating a central ring in the final design. It is also evident that the majority of material tends to concentrate in regions 1 and 2. Minor differences in mass (see Table 4) across analogous cases are due to the relatively large tolerance set for the termination criteria ($\tau = 0.1$). This choice enabled faster convergence of the optimization process without significantly affecting the quality or reliability of the results.

As the thickness of the material surrounding the magnet increases, both the maximum displacement within the magnet and the peak stress in the structure tend to decrease. In terms of equivalent strain, values remain largely consistent across most cases; however, a noticeable increase is observed in the configuration with three layers and the lowest volume fraction due its lower stiffness.

5.3. Parametric model

Here, the objective was to minimize the structural mass ensuring that the displacement of the magnet was below 1 mm, while its strain under 0.5%, and the maximum global stress lower then 800 MPa.

To transition from the TO results to a manufacturable structural concept, a parametric model was developed. The goal was to capture and combine the most relevant geometric features consistently observed across the optimized solutions, such as the presence of reinforcing ribs and the central ring (see Fig. 12).

The parametric model comprised of a Magnet Reinforcement (MR) with two Poloidal Ribs (PRs) at each end, and a Central c-shaped ring (CR), as shown in Fig. 13. Consistent with Section 5.2, one node is constrained in both toroidal and vertical directions, and periodic symmetry were applied.

The key design parameters selected to define the optimal configuration include the Magnet Reinforcement thickness (t_{MR}), the former thickness (t_{former}), the radial thickness of the Central Ring (t_{CR}), and the radial thickness of the ribs (t_{ribs}), while the remaining geometrical

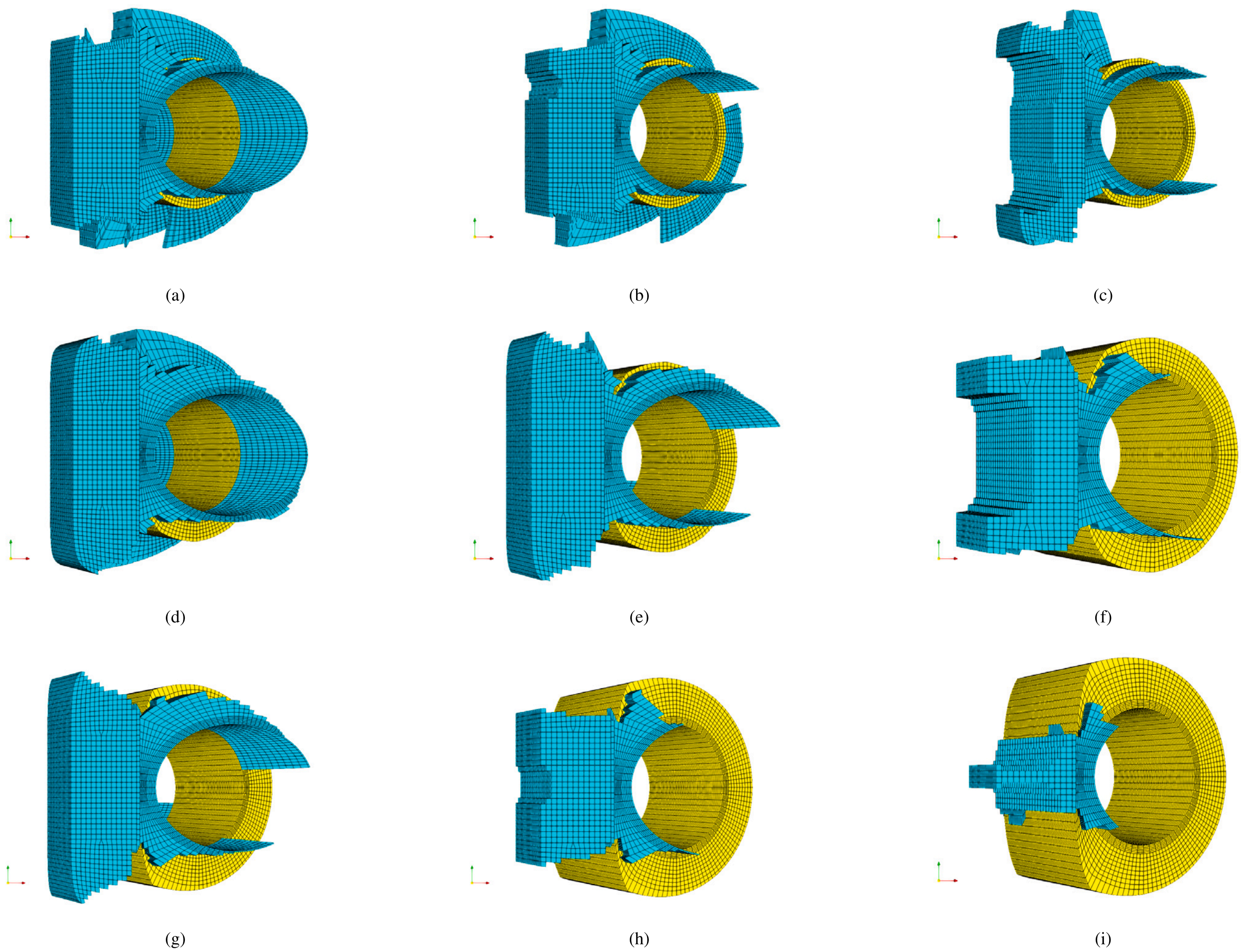

Fig. 12. Topology optimization solutions with volume and extrusion constraints. Figures (a)–(c): 3 layers, volume fractions 50%, 37.5%, 25%; Figures (d)–(f): 6 layers, 45%, 31%, 17%; Figures (g)–(i): 9 layers, 36%, 21%, 5%.

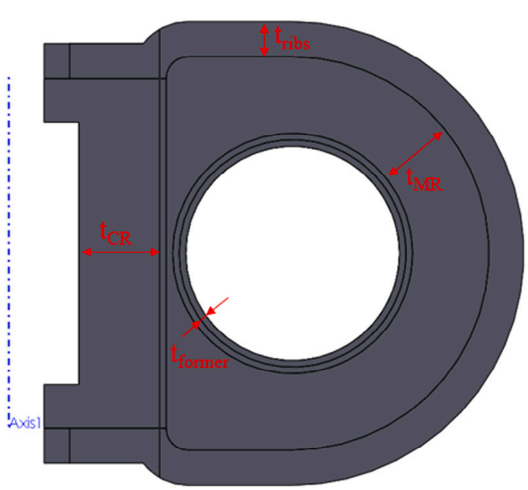

Fig. 13. Lateral view of the parametric model for DoE. t_{MR}: Magnet Reinforcement thickness; t_{former}: former thickness; t_{CR}: Central Ring radial thickness; t_{PR}: Poloidal Ribs radial thickness.

parameters have been set according to the TO solutions (see Fig. 13 for selected parameters).

The impact of the selected parameters on the structural performance was assessed using ANSYS Design of Experiments (DoE), which enabled a systematic exploration of the design space through a series of parametric simulations, facilitating the identification of optimal configurations. The results obtained are shown in the plots of Figs. 14 and 15.

Each solution in Figs. 14 and 15 is referred to a combination of t_{MR}, t_{former}, t_{CR} and t_{ribs}, obtained with the Latin Hypercube Method (LHM). Additional bound limits on the selected variables were included to promote a feasible design. Nearly all evaluated design points satisfied the imposed constraints, with the exception of solution 3, where both maximum displacement and stress slightly exceeded acceptable limits. Among all the evaluated design points, solutions 5 and 18 emerged as the most promising. While solution 18 exhibits marginally higher displacement (0.7 mm vs. 0.5 mm for solution 5) and stress (625 MPa vs. 588 MPa), its equivalent strain remains comparable to that of solution 5 (0.37%). Notably, solution 18 achieves this performance with a reduction of nearly 300 kg in total mass, making it an attractive lightweight alternative.

5.4. Proposed design of magnet's reinforcements

The selected design (solution 18) was refined to ensure well-defined, manufacturable structural features and to prevent any interference with adjacent sectors (see Fig. 16). Specifically, the PRs were positioned slightly inward from the ends to mitigate potential interference caused

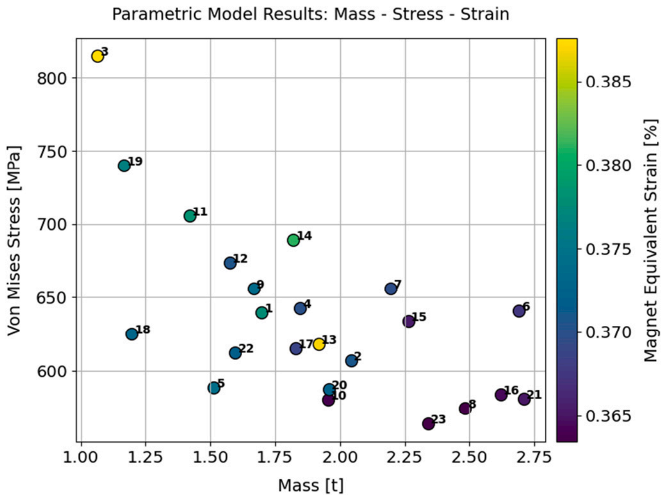

Fig. 14. Results of parametric model in terms of mass (one sector), maximum global stress and maximum magnet strain.

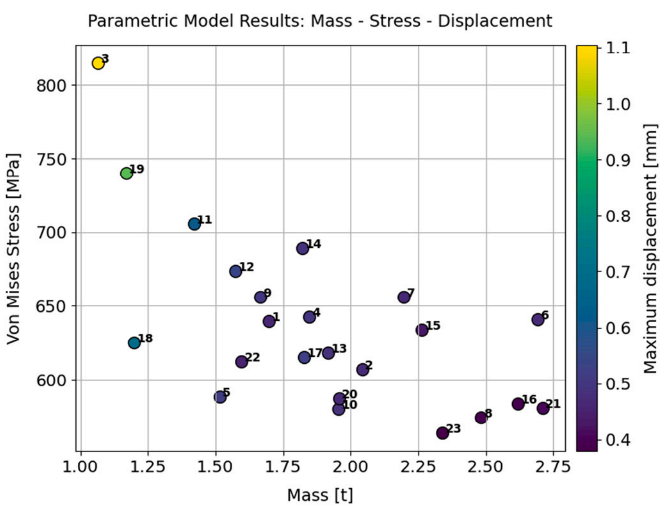

Fig. 15. Results of parametric model in terms of mass (one sector), maximum global stress and maximum magnet displacement.

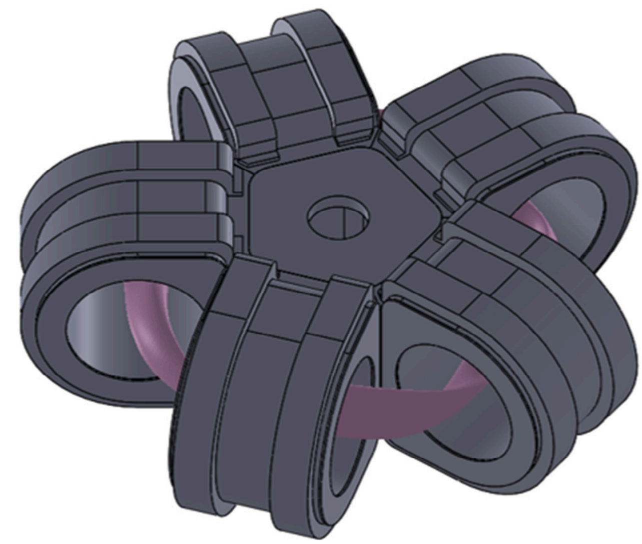

Fig. 16. Representation of the conceptual design of the magnet reinforcements.

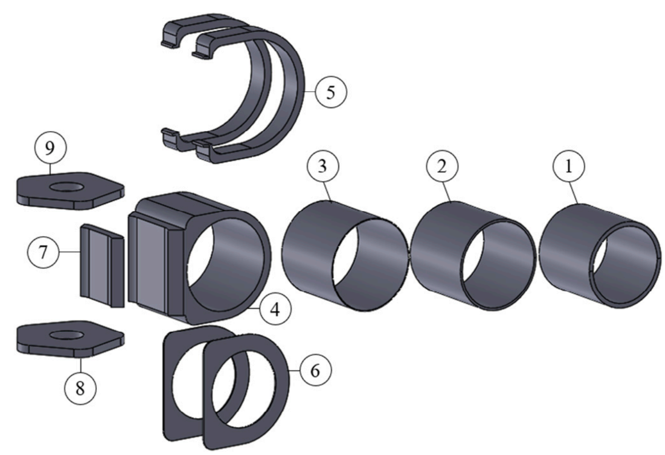

Fig. 17. Exploded view: (1) former, (2) magnet, (3) OC, (4) MR, (5) PRs, (6) former caps, (7) CR vertical plate, (8) CR bottom plate, (9) CR upper plate.

by manufacturing tolerances and deformation during operation. This offset also facilitates assembly: the PRs are intended to be directly welded onto the outer MR surface, but a small clearance is necessary to slide them into place before welding. Therefore, a gap is intentionally provided at both ends of the MR to allow sufficient space for the weld seams.

A central hole was introduced in the CR to ensure tangential continuity, thereby eliminating sharp corners and reducing stress concentrations.

Additionally, two plates were designed to fully enclose the magnet and former, effectively preventing possible axial motion (along magnet axis). The former will be directly connected to these plates through bolted joints, ensuring secure and reliable attachment. A further structural element, referred to as the Outer Cylinder (OC), was introduced to fully enclose and protect the magnet during the fitting operation within the MR.

The thickness of the CR were reduced by increasing the MR thickness towards the machine center, allowing the possibility of assembling the two components using bolted connections. Moreover, the CR were furthermore divided in three main components, that are vertical plates which will be joined with the MR and two upper and bottom horizontal plates. The bottom plate, with a pentagonal shape, will serve as a base for the vertical plates; the two components can be jointed either with bolt connections or weldings. In the first case, the assembly is clearly more modular, however the bolts will carry most of the applied loads. In contrast, the welded connection offers better load distribution due to greater continuity and more effective load sharing across the entire joint.

Lastly, the double symmetry of the MR allows for efficient production via casting. The inner surface, which interfaces with the OC, can be further refined to achieve the required surface roughness.

5.5. Assembly procedure

In this section, we outline a proposed assembly procedure to ensure that all components can be integrated seamlessly and achieve the desired structural integrity under operational conditions. An exploded view of the magnet reinforcements components is depicted in Fig. 17.

The first step consists of winding the wide, engraved HTS tape around a cylindrical former with suitable winding tension. This operation results in the creation of the magnet–inner former unit. Once the winding is complete, the entire assembly is cooled down to facilitate the next step, which involves inserting this unit into the OC. This step requires a slight interference fit to ensure a secure and rigid connection between the components.

After assembling the magnet, inner former, and OC into a unified structure, this composite unit is inserted into the MR. This second insertion can be achieved through either a classical interference fit or a tapered fit. In the case of a conical (tapered) coupling, cooling of the internal components can often be avoided, as the angled surfaces allow insertion by applying an axial force, which generates the required contact pressure between components. The efficiency of this method, however, depends heavily on the taper angle, interference magnitude, and surface roughness. Once inserted, two additional plates are attached to the lateral faces of the module. These plates serve to fully enclose the magnet, thereby minimizing possible axial movement, and mechanically connect the inner former to the MR using bolted joints. The MR also extends toward the machine center to provide sufficient material thickness to host radial bolts used for connecting to the CR.

Following this step, the CR assembly can be performed independently. The CR consists of a bottom pentagonal plate, five vertical plates, and a top plate matching the bottom geometry. These components are joined using either bolted or welded connections, depending on the desired mechanical performance and modularity.

Then, the MR and CR assemblies are connected using radial bolts inserted through the inner sides of the CR's vertical plates. Finally the upper plate is bolted on CR's vertical plates.

Future design could include a larger circular hole for the upper plate, which could be welded with the vertical plates for better structural connection. This should also provide sufficient space for inserting the radial bolts. Another option that could increase the CR stiffness, consists of directly casting all components (vertical, bottom and upper plates), eliminating the need for precise welded connections between the plates.

5.6. FEA of proposed design of magnet's reinforcements

To evaluate the effects of the design changes described in Section 5.4, a FEA was carried using boundary conditions similar to those detailed in Section 5.2, with the exception of the contact definitions used to model the interactions between the OC, the magnet, and the MR. Specifically, a bonded contact was assumed between the magnet and the former, reflecting the presence of tape that will be secured to the former. In contrast, frictional contacts were defined at the interfaces between the OC and the magnet, as well as between the OC and the MR, using a friction coefficient of $\mu_s = 0.15$. A preliminary interference value of $i = 0.05$ mm was assumed in this study for the fit interfaces; however, dedicated analyses are required to determine the optimal interference values to guarantee consistent contact, particularly during cool-down and to avoid separation between components under operational conditions.

The magnet undergoes a maximum displacement of 1.1 mm (see Fig. 18), with a peak strain of 0.50% and a corresponding maximum von Mises stress of 648 MPa (see Fig. 19). The highest stress within the entire assembly occurs in the lateral plates, where the stress reaches up to 870 MPa.

Although the peak stress slightly exceeds the value obtained with the parametric model, it remains below the acceptable limit of 1000 MPa. The magnet displacement, which is nearly two times greater, could be reduced by increasing either the PRs dimensions or the MR thickness. Finally, the magnet strain can be further minimized by increasing the interference fit between components.

6. Conclusion and future works

In this work, a structural optimization framework was developed for the conceptual design of reinforcement structures for a 10 T on axis, 52 cm bore stellarator magnet. The design process began with an initial mass minimization strategy, which led to a significant reduction in the design space, from 11.3 t to 3.93 t. A second round of Topology Optimization, incorporating multiple extrusion constraints, further reduced the mass to 1.65 t and revealed key structural features such as a C-shaped Central Ring (CR), Poloidal Ribs (PRs), and a Magnet Reinforcement (MR). A parametric model was then created based on the second optimization run to explore design variants and refine key parameters, ultimately achieving a final mass of 1.20 t. To accommodate manufacturing and assembly requirements, the design was slightly adjusted without compromising its structural integrity. The final proposed configuration experiences a maximum displacement of 1.1 mm, a peak strain of 0.50%, and a von Mises stress of 648 MPa in the magnet. The highest stress in the assembly, 870 MPa, is reached in the lateral plates. Compared to the initial large-scale design, this approach resulted in a nine-fold reduction in mass, while maintaining acceptable mechanical performance.

Future developments should focus on the detailed design of subcomponents through high-fidelity FEA, including the modeling of bolts, and welds. Additional efforts should be directed toward optimizing interference fits to achieve the desired magnet pre-compression. Another promising direction is the exploration of higher-dimensionality Topology Optimization, for example using beam or truss representations; this could enable to reach lighter structures, while also allowing for asymmetric configurations that may exhibit superior structural performance. A thermo-mechanical analysis under realistic operating conditions is also essential to evaluate potential contact losses or mechanical degradation during cool-down phases and operational conditions.

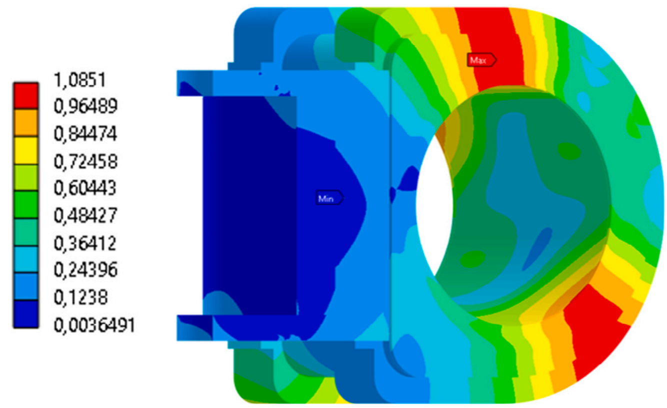

Fig. 18. Displacement field of proposed design [mm].

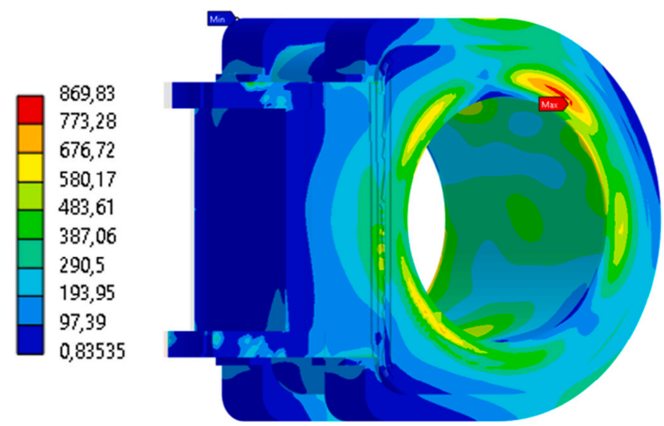

Fig. 19. Stress field of proposed design [MPa].

In the present study, the mechanical response under only the EM loads were considered, which typically governs the early-stage design of the reinforcement structure. Stellarator magnets are generally conceived for steady-state operation; however, for this experimental device, multiple energization cycles will occur due to repeated operation. These cycling loads, which may give rise to fatigue effects, will be included in future iterations of the structural optimization.

Abbreviations

- TO: Topology Optimization
- CAD: Computer Aided Design
- EM: Electro-Magnetic
- HTS: High Temperature Superconductors
- SIMP: Solid Isotropic Material Penalization
- MR: Magnet Reinforcement
- PRs: Poloidal Ribs
- CR: Central Ring
- DoE: Design of Experiments
- LHM: Latin Hypercube Method
- OC: Outer Cylinder
- FEA: Finite Element Analysis

CRediT authorship contribution statement

S. Del Nero: Writing – original draft, Software, Methodology, Conceptualization. **P. Fanelli:** Writing – review & editing, Supervision, Methodology, Conceptualization. **V. Prost:** Writing – review & editing, Supervision, Methodology, Conceptualization. **F.A. Volpe:** Project administration.

Declaration of competing interest

The authors declare the following competing interests: S. Del Nero and P. Fanelli are affiliated with University of Tuscia, and V. Prost and F.A. Volpe are employed by Renaissance Fusion. This research project is jointly funded by University of Tuscia and Renaissance Fusion. This financial support is acknowledged and has not influenced the execution or interpretation of the research. No other competing interests are declared.

Acknowledgments

This publication was produced while attending the Ph.D. program in "Engineering for Energy and Environment" at the University of Tuscia, Cycle XXXVIII, with the support of a scholarship co-financed by the Ministerial Decree no. 352 of 9th April 2022, based on the NRRP - funded by the European Union - NextGenerationEU - Mission 4 "Education and Research", Component 2 "From Research to Business", Investment 3.3 "Introduction of innovative Ph.D. programs that meet the innovation needs of businesses and promote the hiring of researchers by companies".

The authors would also like to thank Gopal Dewangan for his valuable support and continuous feedback, and all the members of the Renaissance Fusion Science team for their helpful input and insightful discussions throughout the project.

Data availability

The Topology Optimization code developed for this study is available from the corresponding author upon request. We strongly support knowledge sharing within the research community, as it is essential for transparency, reproducibility, and advancing the boundaries of current methodologies.

References

[1] J. Zhu, W. Zhang, L. Xia, Topology optimization in aircraft and aerospace structures design, Arch. Comput. Methods Eng. (2015) http://dx.doi.org/10.1007/s11831-015-9151-2.

[2] O. Okorie, A. Perveen, D. Talamona, K. Kostas, Topology optimization of an aerospace bracket: Numerical and experimental investigation, Appl. Sci. 13 (24) (2023).

[3] K.D. Tsavdaridis, Applications of topology optimization in structural engineering: High-rise buildings and steel components, Jordan J. Civ. Eng. 9 (3) (2015) 335–357, http://dx.doi.org/10.14525/jjce.9.3.3076.

[4] A. Sutradhar, J. Park, P. Haghighi, D. Detwiler, J. Shah, Incorporating manufacturing constraints in topology optimization methods: A survey, 2017, V001T02A073, http://dx.doi.org/10.1115/DETC2017-68192.

[5] S. Vatanabe, T. Lippi, C. R. de Lima, G. Paulino, E. Silva, Topology optimization with manufacturing constraints: A unified projection-based approach, Adv. Eng. Softw. 100 (2016) 97–112, http://dx.doi.org/10.1016/j.advengsoft.2016.07.002.

[6] H. Tamura, T. Goto, J. Miyazawa, T. Tanaka, N. Yanagi, Seismic analysis of magnet systems in Helical fusion reactors designed with topology optimization, IEEE Trans. Appl. Supercond. 32 (6) (2022) 1–4.

[7] C. Zhu, K. Hammond, T. Brown, D. Gates, M. Zarnstorff, K. Corrigan, M. Sibilia, E. Feibush, Topology optimization of permanent magnets for stellarators, Nucl. Fusion 60 (10) (2020) 106002, http://dx.doi.org/10.1088/1741-4326/aba453.

[8] O. Marshall, L. Margetts, L. E., M. Roy, Thermal topology optimisation of a plasma facing component for use in Next-Generation fusion reactors, 2021.

[9] B. Curzadd, A. von Müller, R. Neu, U. von Toussaint, Topology optimization of tungsten/copper structures for plasma-facing component applications, Nucl. Fusion 59 (8) (2019) 086003, http://dx.doi.org/10.1088/1741-4326/ab1ff5.

[10] M. Baelmans, M. Blommaert, W. Dekeyser, T. Van Oevelen, Achievements and challenges in automated parameter, shape and topology optimization for divertor design, Nucl. Fusion 57 (3) (2017) 036022, http://dx.doi.org/10.1088/1741-4326/57/3/036022.

[11] F. Schauer, K. Egorov, V. Bykov, HELIAS 5-B magnet system structure and maintenance concept, Fusion Eng. Des. 88 (9) (2013) 1619–1622, http://dx.doi.org/10.1016/j.fusengdes.2013.01.035, Proceedings of the 27th Symposium On Fusion Technology (SOFT-27); Liège, Belgium, September 24-28, 2012.

[12] J. Lion, J.-C. Anglès, L. Bonauer, A. Bañón Navarro, S. Cadena Ceron, R. Davies, M. Drevlak, N. Foppiani, J. Geiger, A. Goodman, W. Guo, E. Guiraud, F. Hernández, S. Henneberg, R. Herrero, C. Hintze, H. Höchter, J. Jelonnek, F. Jenko, R. Jorge, M. Kaiser, M. Kubie, E. Lascas Neto, H. Laqua, M. Leoni, J. Lobsien, V. Maurin, A. Merlo, D. Middleton-Gear, M. Pascu, G. Plunk, N. Riva, M. Savtchouk, F. Sciortino, J. Schilling, J. Shimwell, A. Di Siena, R. Slade, T. Stange, T. Todd, L. Wegener, F. Wilms, P. Xanthopoulos, M. Zheng, Stellaris: A high-field quasi-isodynamic stellarator for a prototypical fusion power plant, Fusion Eng. Des. 214 (2025) 114868, http://dx.doi.org/10.1016/j.fusengdes.2025.114868.

[13] F. Schauer, H. Wobig, K. Egorov, V. Bykov, M. Köppen, Extrapolation of the W7-X magnet system to reactor size, Contrib. Plasma Phys. 50 (8) (2010) 750–755, http://dx.doi.org/10.1002/ctpp.200900011.

[14] A. Kaszynski, pyansys: Pythonic interface to MAPDL, 2021, http://dx.doi.org/10.5281/zenodo.4009466.

[15] Renaissance Fusion Official Website, https://renfusion.eu. (Accessed June 2025).

[16] D. Botelho, V. Prost, L. Pereira, F. Volpe, Simplified magnet design and manufacture based on patterning of wide conductors, 2024, http://dx.doi.org/10.48550/arXiv.2409.20143.

[17] Max-Planck-Institute for Plasma Physics, Wendelstein 7-X, https://www.ipp.mpg.de/w7x. (Accessed September 2025).

[18] B. Wang, Y. Zhou, K. Tian, G. Wang, Novel implementation of extrusion constraint in topology optimization by Helmholtz-type anisotropic filter, Struct. Multidiscip. Optim. 62 (2020) http://dx.doi.org/10.1007/s00158-020-02597-1.

[19] J. Ma, Y. He, Z.-L. Zhao, Y.M. Xie, Topology optimization of ribbed slabs and shells, Eng. Struct. 277 (2023) 115454, http://dx.doi.org/10.1016/j.engstruct.2022.115454.

[20] M.P. Bendsøe, O. Sigmund, Material interpolation schemes in topology optimization, Arch. Appl. Mech. 69 (9) (1999) 635–654, http://dx.doi.org/10.1007/s004190050248.

[21] S.D. Nero, P. Fanelli, V. Prost, S. Meloni, Element-based connectivity approach for topology optimization of Rib Layout Design, 2025, Accepted for publication in Structural and Multidisciplinary Optimization.

[22] M. Iguchi, T. Sakurai, M. Nakhira, N. Koizumi, H. Nakajima, Cryogenic structural materials of the ITER toroidal field coil structure, in: Fourth International Workshop on Structural Materials for Innovative Nuclear Systems (SMINS-4), Nuclear Energy Agency, Paris, France, 2016.

[23] Y. Zhang, REBCO tape production at SuperPower: state of the art and prospects, in: 1st High Temperature Superconductor Accelerator Technology (HiTAT) Workshop, CERN, 2023, Presented on March 9, 2023.

[24] H. Milanchian, S.B. Balani, T. Salmi, Mechanical simulation of 2G HTS tapes and stacks during localized temperature increase, IEEE Trans. Appl. Supercond. 35 (5) (2025) 1–6, http://dx.doi.org/10.1109/TASC.2025.3548635.

[25] R. Schapery, Thermal expansion coefficients of composite materials based on energy principles, J. Compos. Mater. 2 (3) (1968) 380–404, http://dx.doi.org/10.1177/002199836800200308.

[26] W. Zhou, B. Su, R. Jia, J. Cao, Electro-magnetic-mechanical characteristics of 3D HTS INS and NI racetrack coils in complex physical fields, Cryogenics 145 (2025) 104003, http://dx.doi.org/10.1016/j.cryogenics.2024.104003.

[27] Y. Wang, Z. Jing, Multiscale modelling and numerical homogenization of the coupled multiphysical behaviors of high-field high temperature superconducting magnets, Compos. Struct. 313 (2023) 116863, http://dx.doi.org/10.1016/j.compstruct.2023.116863.